Article

# Te Substitution-Induced Structural Evolution and Thermoelectric Properties of Quasi-1D BiSeI

**Zhiyao Zhang [1,2], Zuyong Feng [1,\*] and Jian Zhou [2,\*]**

[1] School of Physics and Optoelectronic Engineering, Guangdong University of Technology, Guangzhou 510006, China; zhiyaozhang08@gmail.com (Z.Z.)

[2] School of Materials Science and Engineering, State Key Laboratory of Optoelectronic and Technology, Key Laboratory for Polymeric Composite and Functional Materials of Ministry of Education, Guangzhou Key Laboratory of Flexible Electronic Materials and Wearable Devices, Laboratory of Advanced Electronics and Fiber Materials, Sun Yat-sen University, Guangzhou 510275, China

\* Corresponding author. E-mail: fengzuyong@gdut.edu.cn (Z.F.); zhouj296@mail.sysu.edu.cn (J.Z.)

**ABSTRACT:** Halide-chalcogenide compounds are promising candidates for thermoelectric applications owing to their low thermal conductivity and tunable electronic structures. Here, we systematically investigate Te-substituted $BiSe_{1-x}Te_xI$ (x = 0, 0.1, 0.3, 0.5). Structural and spectroscopic analyses confirm the successful incorporation of Te into the BiSeI-type framework, accompanied by lattice expansion, vibrational softening, and pronounced bandgap tuning. X-ray photoelectron spectroscopy verifies that Te occupies Se sites and modifies the local electronic environment, while electron microscopy reveals a morphology evolution from ribbon-like grains to plate-like and fragmented particles with increasing Te content. Thermoelectric measurements show that Te substitution simultaneously enhances electrical conductivity and suppresses thermal conductivity, arising from band-structure modulation, increased carrier concentration, mass fluctuation, and strengthened phonon scattering. Consequently, $BiSe_{0.7}Te_{0.3}I$ achieves the highest $ZT$ (~0.27 at 400 K), substantially higher than pristine BiSeI. This work demonstrates that heavy-element doping is an effective strategy for optimizing the thermoelectric performance of halide-chalcogenides.

**Keywords:** Layered halide-chalcogenides; Heavy-element doping; Bandgap narrowing; Thermoelectric performance

## 1. Introduction

Thermoelectric (TE) materials enable solid-state heat–electricity conversion, and their efficiency is quantified by the dimensionless figure of merit $ZT = S^2\sigma T/\kappa$, where $S$ is the Seebeck coefficient, $\sigma$ is the electrical conductivity, and $\kappa$ is the total thermal conductivity. Achieving high $ZT$ therefore requires the simultaneous realization of a large power factor $S^2\sigma$ (high $\sigma$ together with a large $|S|$) and a low $\kappa$, particularly a strongly suppressed lattice component $\kappa_l$. However, these transport parameters are inherently coupled: increasing carrier concentration usually enhances $\sigma$ but reduces $|S|$ and increases the electronic contribution to $\kappa$, making it essential to coordinate band and carrier-concentration engineering with phonon-

transport control [1–4]. Additionally, materials exhibiting strong anharmonicity and structural anisotropy can achieve intrinsically low $\kappa_l$. A prominent example is single-crystal SnSe, which has achieved record-high *ZT* values above room temperature due to its ultralow intrinsic $\kappa_l$ and pronounced anisotropic thermal transport, serving as a benchmark for optimizing structure-thermal transport coupling [5]. Building on this concept, recent advances in multi-anion layered superlattices have established a generalizable strategy for achieving low thermal conductivity. For example, $Bi_4O_4SeCl_2$ integrates both strong and weak chemical bonds along with atomic size mismatch within a single structural unit, resulting in a room-temperature $\kappa$ of ~0.10 $W \cdot m^{-1} \cdot K^{-1}$ along the stacking direction by simultaneously suppressing longitudinal and transverse phonon modes at the unit cell level [6]; Its 1:1 modular superlattice structure ($Bi_2O_2Se/BiOCl$) preserves favorable electronic band structures and carrier mobility while enabling dimensional confinement effects [7]. Furthermore, this material exhibits stable tightly bound excitons (~375 meV) and a degenerate carrier concentration of ~$1.25 \times 10^{19}$ $cm^{-3}$ at room temperature, demonstrating the coexistence of ultralow thermal conductivity and superior electrical transport properties [8]; Upon extension of this family to $Bi_4O_4SeBr_2$ and $Bi_6O_6Se_2Cl_2$, the systems retain exceptionally low $\kappa$ values and exhibit tunable doping characteristics, offering a versatile platform for the coupled regulation of thermal and electronic transport [9].

For system improvements targeting *ZT* enhancement, four complementary strategies are typically employed: (i) Coordinated optimization of carrier concentration and mobility, achieved through acceptor/donor doping, defect engineering, and band filling to regulate the "optimal operating point" of the power factor ($PF = S^2\sigma$); (ii) Band engineering, which involves energy valley degeneracy or convergence, effective mass modulation, and the introduction of resonant energy levels to increase the density-of-states effective mass while preserving carrier mobility; (iii) Phonon engineering, aimed at constructing multiscale phonon scatterers-ranging from point defects and dislocations to secondary phases and nanointerfaces-to achieve broadband phonon scattering and thereby reduce lattice thermal conductivity ($\kappa_l$); (iv) Texture, orientation, and strain engineering, particularly effective in layered or anisotropic materials, where thermomechanical processing enables preferential alignment to suppress cross-plane thermal conductivity and enhance the continuity of charge transport pathways, often combined with high-entropy solid solutions to improve structural stability [10–14]. Among these approaches, heavy-element doping within the framework of "electron-phonon bidirectional coupling" offers distinct advantages. On the one hand, according to Klemens' point-defect scattering theory and its later extensions, the introduction of heavy atoms with large mass and size mismatches creates pronounced mass contrast and local strain fields. These perturbations enhance the scattering of mid- to high-frequency phonons, soften the lattice, and lower the sound velocity, thereby substantially reducing the lattice thermal conductivity ($\kappa_l$). This mechanism has been consistently validated in semiconductor alloys, chalcogenides, and half-Heusler materials [15–18]. On the other hand, the strong spin-orbit coupling and extended p-orbitals characteristic of heavy elements enable fine control over the band structure, including adjustments to the bandgap and band edge positions, potentially inducing valley convergence or forming resonant levels that produce local peaks in the density of states. These effects can simultaneously enhance the Seebeck coefficient (*S*) and electrical conductivity ($\sigma$), thereby increasing PF without severely compromising mobility. Notable examples include Tl-induced resonant levels and valley convergence in PbTe, as well as recent advances in $Mg_3(Sb, Bi)_2$ and half-Heusler systems within this paradigm [19–21]. Furthermore, heavy-element doping can be integrated with nanostructured or dislocation-engineered architectures, creating hierarchical scattering centers spanning point defects, interfaces, and dislocations-exemplified by the PbTe-SrTe system, which significantly suppresses $\kappa_l$. Similarly, texture development and thermal deformation in layered $Bi_2Te_3$ have demonstrated concurrent improvements in *PF* and mechanical robustness within the operational temperature range of practical devices [11,14]. Beyond these established TE paradigms, low-dimensional van der Waals chalcogenides and topological materials provide instructive examples of how structural anisotropy and strong spin–orbit coupling can concurrently shape charge and heat transport. For instance, $Bi_2Se_3$, a

prototypical layered topological insulator, has recently been synthesized via an edge-dominated, flow-confined epitaxy strategy, yielding large-area, high-quality films with ultrabroadband response [22]. Elemental tellurium (Te), composed of covalently bonded atoms arranged in helical chains and packed through van der Waals interactions, has also emerged as a versatile narrow-bandgap semiconductor: cryogenically evaporated ultrathin Te films enable wafer-scale *p*-type FETs with high effective hole mobility and robust switching characteristics [23], while tellurene has been reported to exhibit a giant infrared bulk photovoltaic effect enabling broad-spectrum functionality [24]. In a related bismuth-based mixed-anion chalcohalide, *n*-type $Bi_{13}S_{18}Br_2$ leverages a Fajans'-polarization-driven subvalent $[Bi_2]^{4+}$ twin-rattler that simultaneously introduces donor states near $E_F$ and intensifies phonon scattering, thereby enabling a high intrinsic thermoelectric performance ($ZT \approx 1.0$ at 748 K) [25]. These representative chalcogenide systems underscore that anisotropic bonding hierarchies, heavy-element chemistry, and microstructure control are powerful levers for decoupling electronic and phononic transport, motivating the exploration of mixed-anion chalcohalides such as BiSeI.

BiSeI (bismuth selenoiodide) is a member of the bismuth chalcohalide/oxyhalide family, characterized by layered or quasi-one-dimensional structural motifs and relatively high dielectric constants. It inherently exhibits low lattice thermal conductivity alongside a tunable electronic structure-properties that are highly advantageous for thermoelectric applications-and has also garnered interest for use in optoelectronic devices [26–28]. For thermoelectric purposes, first-principles studies predict ultralow intrinsic $\kappa_l$ in BiSeI and suggest promising performance in the near-ambient to mid-temperature range; however, limited electrical transport ($\sigma$) remains the key bottleneck for further *ZT* improvement, motivating doping/alloying to enhance carrier transport and modestly adjust the band gap [29,30]. Similarly, the isostructural compound BiSI demonstrates exceptionally low $\kappa_l$, underscoring the inherent structural tendency of chalcohalides to suppress phonon-mediated heat transport and emphasizing the importance of optimizing electronic transport properties [27,31]. Advances in low-temperature anion-exchange synthesis methods have facilitated access to phase-pure chalcohalide materials, enabling subsequent doping and microstructural engineering [32]. In this context, heavy-element substitution of tellurium (Te) for selenium (Se) at the selenium site in BiSeI offers an auspicious approach: Te incorporation can tune the band gap and carrier concentration while introducing strong point-defect scattering. At the same time, such substitution is expected to disturb the original belt-like BiSeI morphology and promote microstructural disorder, providing additional phonon-scattering centers beyond simple point defects. However, systematic investigations of Te-for-Se substitution in BiSeI, especially the correlation between Te-induced structural evolution and thermoelectric transport, remain lacking.

In this work, we systematically investigate the structural, optical, and thermoelectric properties of $BiSe_{1-x}Te_xI$ (x = 0, 0.1, 0.3, 0.5). Structural characterizations confirm the successful substitution of Se by Te, accompanied by lattice expansion, vibrational softening, and enhanced disorder, while the BiSeI-type phase is retained. Optical measurements demonstrate that Te incorporation effectively tunes the band gap, and XPS spectra evidence a modified local electronic environment around Bi-(Se/Te). SEM and TEM analyses reveal a pronounced morphology evolution from large ribbon-like grains in BiSeI to plate-like and fragmented particles in Te-doped samples. Most importantly, thermoelectric measurements show that Te substitution significantly enhances electrical conductivity while reducing thermal conductivity, thereby improving *ZT*. This study not only establishes the structure-property relationship in $BiSe_{1-x}Te_xI$ but also highlights the effectiveness of Te alloying in optimizing thermoelectric performance in halide-chalcogenides. The findings provide valuable insights for the rational design of high-performance thermoelectric and optoelectronic materials based on mixed-anion systems.

## 2. Experimental Section

### 2.1. Solid-Phase Synthesis

The synthesis of $BiSe_{1-x}Te_xI$ (x = 0, 0.1, 0.3, 0.5) was carried out by solid-phase reaction. Stoichiometric amounts of Bi powder, Se powder, Te powder, and $I_2$ granules were mixed and ground using an agate mortar. The homogeneous mixture was then sealed in an evacuated quartz ampoule and placed in a muffle furnace (KSL-1200X-M, HEFEI KEJING, Hefei, China). The sample was heated at 5 °C/min to 550 °C, held at this temperature for 24 h, and then naturally cooled to room temperature to obtain polycrystalline $BiSe_{1-x}Te_xI$ (x = 0, 0.1, 0.3, 0.5). The resulting powder was ground again and then pressed into two types of compacts using an infrared tablet press (YLJ-40TA, HEFEI KEJING, Hefei, China): cylindrical pellets with a radius of 10 mm and rectangular bars with dimensions of 10 mm × 3 mm, both under a pressure of 30 MPa, for subsequent characterization.

### 2.2. Structural and Morphological Characterization

X-ray diffraction (XRD) was performed in a continuous mode using a PANalytical X-ray diffractometer (Malvern Panalytical, Malvern, UK) with Cu Kα radiation (λ = 1.5406 Å) at 40 kV and 15 mA. The material band gap was characterized by UV-Vis-NIR absorption spectroscopy (Shimadzu UV-3600i Plus, Shimadzu, Japan). The X-ray photoelectron spectroscopy (XPS) spectra were obtained using a K-alpha spectrometer (Thermo Scientific Inc, Waltham, MA, USA) with Al Kα (1486.6 eV) radiation. Morphological analysis of the samples was performed using cold-field-emission scanning electron microscopy (SEM, SU8010, Hitachi, Chiyoda, Japan). Transmission electron microscopy (TEM) images were acquired using a Talos F200X G2 instrument (Thermo Fisher Scientific, Waltham, MA, USA) operated at 200 kV. The electrical conductivity ($\sigma$) and Seebeck coefficient ($S$) were measured using a NAMICRO-II thermoelectric parameter measurement system on rectangular specimens with dimensions of 10 mm × 3 mm × (3–5) mm (length × width × height). During the measurements, one end of the sample was heated to establish a slight temperature gradient (typically 10–20 K), and both the temperature difference and corresponding thermoelectric voltage were recorded to determine the Seebeck coefficient. Simultaneously, electrical conductivity was measured using the standard four-probe method integrated into the system. The thermal conductivity ($\kappa$) was determined at various temperatures using a Hot Disk TPS2500S thermal constant analyzer (Hot Disk AB, Gothenburg, Sweden). During the measurements, cylindrical samples with a 10 mm radius were used. The Hot Disk method uses a nickel double-spiral sensor that serves as both a heat source and a temperature detector. The sensor was sandwiched between two identical sample halves to ensure good thermal contact and minimize heat loss. Each measurement was conducted three times at every testing temperature to ensure reproducibility and reliability of the data, and the average value was taken as the final thermal conductivity ($\kappa$) for that temperature point. All thermoelectric measurements were performed on cold-pressed compacts prepared under identical conditions (30 MPa), with the same die diameter and thickness. Hall effect measurements were performed on an Ecopia HMS-7000 system to determine the carrier concentration and mobility of $BiSe_{1-x}Te_xI$.

## 3. Results and Discussion

### 3.1. Structural and Vibrational Analysis

BiSeI crystallizes in the orthorhombic crystal system (*Pnma* space group) and adopts a quasi-one-dimensional ribbon-like structure, in which its chains/ribbons run along the crystallographic *b*-axis and are separated by iodine atoms through weak van der Waals interactions, giving rise to pronounced anisotropy in its physical properties. Each Bi atom is coordinated by four selenium atoms and two iodine atoms in a nearly octahedral manner, forming strong covalent bonds within the layer and weak van der Waals

interactions between layers. This "strong within layers and weak between layers" bonding hierarchy not only endows the material with excellent peelability but also results in extremely low intrinsic lattice thermal conductivity [31]. In terms of electronic structure, BiSeI is a narrow-bandgap semiconductor with an optical bandgap of approximately 1.3–1.5 eV [28]. Se 4p orbitals mainly contribute to the valence band top, while the conduction band bottom is dominated by Bi 6p orbitals, demonstrating a distinct p-p orbital hybridization feature [33]. To investigate the structural evolution and phase stability of $BiSe_{1-x}Te_xI$ upon tellurium incorporation, a systematic characterization of the synthesized samples was conducted using crystallographic analysis, solid-state synthesis, X-ray diffraction (XRD), and Raman spectroscopy, as illustrated in Figure 1. Figure 1a–c depict the crystal structure of a representative composition, $BiSe_{0.7}Te_{0.3}I$, viewed along different crystallographic directions. The three-dimensional coordination environment (Figure 1a) shows that bismuth atoms are coordinated to chalcogenide (Se/Te) and iodine atoms in a layered arrangement. The side view along the *a–c* plane (Figure 1b) highlights the alternating stacking of Bi–Se (Te) and I atomic layers, confirming the anisotropic nature of the crystal structure. The top view along the *c*-axis (Figure 1c) further illustrates the in-plane atomic configuration, in which Te atoms partially occupy Se sites without disrupting the periodicity or symmetry of the parent BiSeI framework. To provide a more comprehensive structural comparison across compositions, multi-view crystal models of $BiSe_{1-x}Te_xI$ (x = 0, 0.1, 0.5) are displayed in Figure S1, which complements Figure 1a–c. The three-dimensional, side, and top projections clearly show that all samples preserve the characteristic quasi-one-dimensional Bi–Se–I framework, with Te atoms occupying Se sites isovalently. From BiSeI to $BiSe_{0.9}Te_{0.1}I$ and $BiSe_{0.5}Te_{0.5}I$, the overall lattice periodicity and stacking configuration remain intact, indicating that Te incorporation does not disrupt the intrinsic anisotropic crystal structure but slightly modifies the local coordination environment. The comparative visualizations in Figures 1 and S1 collectively confirm that Te substitution preserves the characteristic quasi-one-dimensional Bi–Se–I ribbon framework while subtly modifying the inter-ribbon distances and bonding characteristics.

The synthetic procedure for $BiSe_{1-x}Te_xI$ (x = 0, 0.1, 0.3, 0.5) is schematically presented in Figure 1d. The compounds were prepared via a conventional solid-state reaction method, wherein stoichiometric amounts of elemental Bi, Se, Te, and I were sealed in evacuated quartz ampoules and annealed at 550 °C for 24 h. This simple, single-step approach enables uniform incorporation of tellurium while preserving phase purity, offering a scalable route for the synthesis of tellurium-doped BiSeI derivatives. To evaluate the phase composition and crystallinity of the resulting materials, Powder X-ray diffraction (XRD) measurements were performed (Figure 1e). The major reflections of all samples can be indexed to the orthorhombic BiSeI-type phase (ICSD No. 133377), indicating that the BiSeI-type framework is retained as the dominant phase upon Te substitution. Meanwhile, a few weak extra reflections (marked with *) appear in Te-substituted samples, suggesting the presence of a trace secondary phase. Importantly, selected reflections exhibit a systematic shift toward lower angles with increasing Te content (see enlarged patterns in Figure S2), consistent with lattice expansion due to Te-for-Se substitution. Further structural insights were obtained through Raman spectroscopic analysis (Figure 1f). The pristine BiSeI sample exhibits three characteristic phonon modes at approximately 70.8, 129.4, and 172.2 $cm^{-1}$. As Te content increases, all Raman-active modes exhibit a progressive redshift, indicative of lattice softening and increased atomic mass due to Te substitution. These spectral shifts confirm the successful integration of Te into the BiSeI lattice and the consequent modulation of vibrational dynamics.
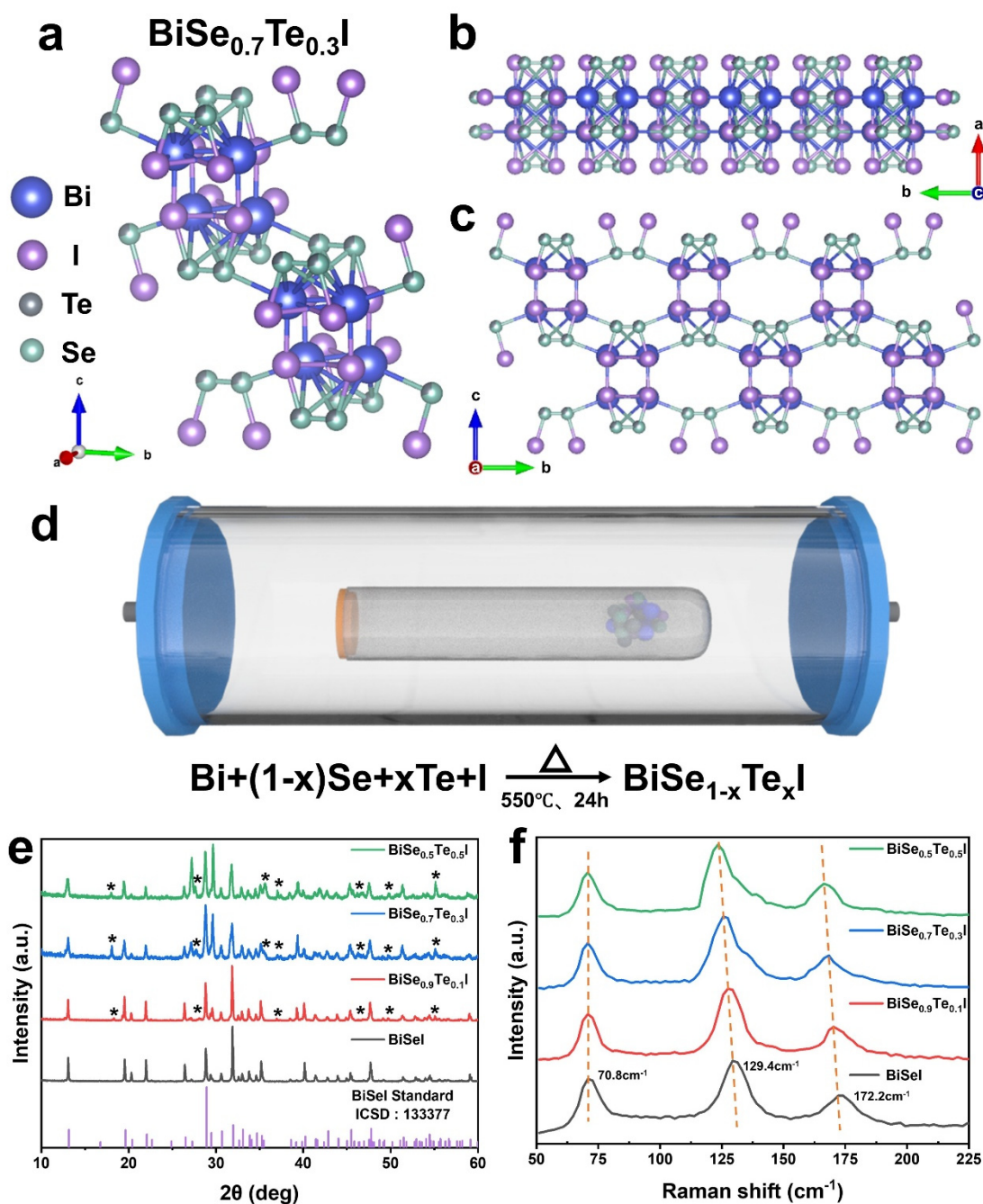
**Figure 1.** Structural models, synthesis process, and phase characterization of $BiSe_{1-x}Te_xI$ (x = 0, 0.1, 0.3, 0.5). (**a**–**c**) Crystal structures of $BiSe_{0.7}Te_{0.3}I$ viewed along different crystallographic directions: (**a**) Three-dimensional view showing the coordination of Bi with (Se/Te) and I; (**b**) side view along the *a*–*c* plane showing the alternately stacked Bi–Se (Te) and I atomic layers; (**c**) top view along the *c*-axis displaying the in-plane atomic arrangement. The atoms are represented by spheres of different colors: Bi (blue), I (purple), Te (gray), and Se (cyan). (**d**) Schematic illustration of the synthesis of $BiSe_{1-x}Te_xI$ through the solid-state reaction method. Stoichiometric amounts of Bi, Se, Te, and I are sealed in an evacuated quartz ampoule, followed by heating at 550 °C for 24 h to obtain the target product $BiSe_{1-x}Te_xI$ via solid-state reaction. (**e**) Powder X-ray diffraction (XRD) patterns of $BiSe_{1-x}Te_xI$ with different Te contents, compared with the standard BiSeI reference (ICSD No. 133377). The major diffraction peaks of all samples match the orthorhombic BiSeI-type structure, indicating that the BiSeI-type phase is retained as the dominant phase upon Te substitution. A few weak extra reflections (marked with *) are observed in Te-substituted samples, suggesting the presence of a trace secondary phase. Selected reflections shift systematically toward lower angles as the Te content increases. (**f**) Raman spectra of $BiSe_{1-x}Te_xI$ samples. The characteristic vibration modes of BiSeI at approximately 70.8, 129.4, and 172.2 cm$^{-1}$ shift gradually toward lower wavenumbers with increasing Te content, reflecting lattice expansion and mass effects induced by Te incorporation.

## 3.2. Optical Bandgap Narrowing and Chemical State Analysis

The optical absorption spectra and corresponding Tauc plots (Figure 2a–d) reveal that the bandgap of BiSeI decreases progressively upon Te substitution, reducing from 1.27 eV for pristine BiSeI to 1.10 eV and 0.98 eV for $BiSe_{0.9}Te_{0.1}I$ and $BiSe_{0.7}Te_{0.3}I$, respectively. Interestingly, a slight increase to 0.99 eV is observed at $BiSe_{0.5}Te_{0.5}I$, as summarized in Figure S2, which is consistent with previously reported values for BiSeI-based systems (1.32 eV) [33]. This nonmonotonic evolution reflects the competing structural and electronic effects of Te incorporation. At moderate substitution levels, Te atoms expand the lattice and modify the electronic potential landscape, effectively narrowing the bandgap through orbital hybridization between Bi-6p and Te-5p states. However, excessive Te content introduces local strain and disorder, partially counteracting this narrowing effect and slightly widening the bandgap again.
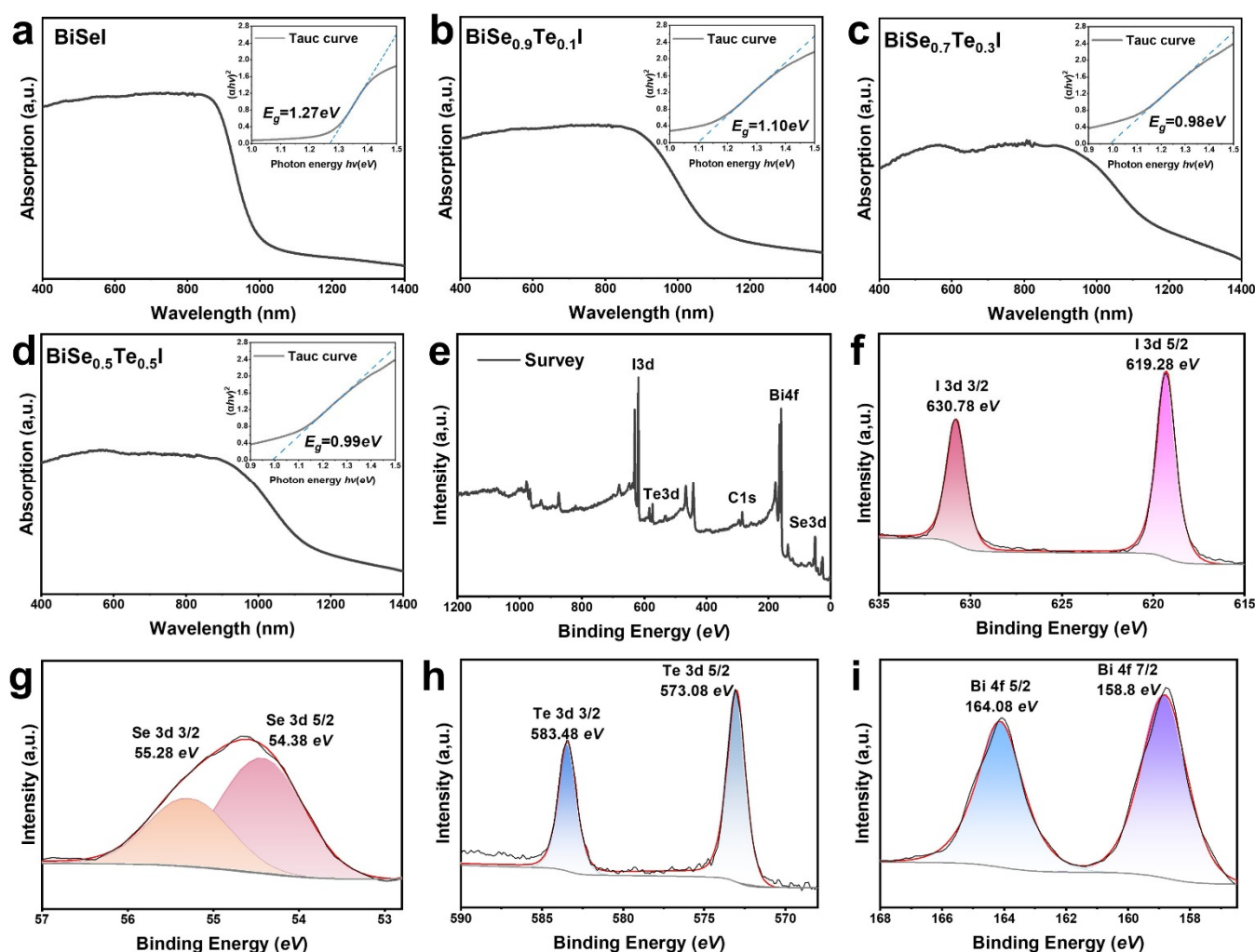


**Figure 2.** Optical absorption and XPS analysis of $BiSe_{1-x}Te_xI$ (x = 0, 0.1, 0.3, 0.5). (**a–d**) UV-Vis-NIR absorption spectra and corresponding Tauc plots of $BiSe_{1-x}Te_xI$ samples. The optical bandgap gradually decreases from pristine BiSeI to Te-rich compositions, indicating modulation of the band structure by Te substitution. (**e**) XPS survey spectra confirming the presence of Bi, Se, Te, and I elements. (**f**) High-resolution XPS spectra of I 3d, showing the characteristic doublet peaks corresponding to I⁻ states. (**g**) High-resolution XPS spectra of Se 3d, revealing the binding energies of $Se^{2-}$ in BiSeI and its shift upon Te incorporation. (**h**) High-resolution XPS spectra of Te 3d, verifying the successful substitution of Te atoms at Se sites. (**i**) High-resolution XPS spectra of Bi 4f, assigned to $Bi^{3+}$ states, confirming the chemical stability of Bi in the lattice. In figures (**f–i**), the black lines represent the experimental spectra, the red lines denote the overall fitting curves, the gray lines correspond to the background signals, and the colored shaded peaks indicate the deconvoluted component peaks.

The consistent trend observed in Figures 2 and S2 clearly demonstrates that Te substitution in BiSeI induces a controlled modulation of the electronic structure. The bandgap narrowing at low-to-moderate doping levels is primarily due to enhanced overlap between Bi-p and (Se/Te)-p orbitals, whereas the subsequent saturation or reversal at high Te content arises from lattice distortion and defect-induced carrier localization. This interplay between structural expansion and electronic reconfiguration strikes a fine balance between improved conductivity and preserved band structure, which is crucial for optimizing thermoelectric performance.

Complementary XPS survey spectra (Figure 2e) confirm the coexistence of Bi, Se, Te, and I elements, and the high-resolution spectra (Figure 2f–i) provide further insights into the chemical states. The I 3d peaks are resolved at 630.78 eV and 619.28 eV, corresponding to $I^-$ states (Figure 2f). The Se 3d peaks at 55.28 eV and 54.38 eV verify the $Se^{2-}$ state and show a distinct shift after Te doping (Figure 2g). Meanwhile, the Te 3d spectra (Figure 2h) confirm the successful incorporation of Te atoms at Se sites, and the Bi 4f spectra (Figure 2i) can be assigned to $Bi^{3+}$, demonstrating the chemical stability of Bi within the lattice. Together, these results highlight the tunability of the optical bandgap and the robust elemental stability of $BiSe_{1-x}Te_xI$ solid solutions.

## 3.3. Morphology and Structural Disorder under Te Incorporation

Beyond the bandgap modulation and chemical-state stability described above, Te substitution also induces pronounced changes in the particle morphology and elemental distribution of BiSeI-based powders. The original BiSeI powder consists of large, smooth, banded crystals with high aspect ratio and distinct edges (Figure S3a,b), exhibiting a one-dimensional banded morphology. As the doped Te content increases, the morphology of the BiSeI-based powder evolves distinctly. When a small amount of Te is introduced ($BiSe_{0.9}Te_{0.1}I$), the original banded structure cracks significantly, and some parts break into thick plates (Figure S3c,d). The particles are still relatively large, but their surfaces show more steps and fracture features, indicating that the incorporation of Te has begun to weaken the mechanical integrity of the bands. With further increasing Te content to x = 0.3, the $BiSe_{0.7}Te_{0.3}I$ powder is dominated by two-dimensional plate-like particles and smaller debris (Figure 3a,b). These plates are much shorter and thicker than the original belts, and their edges are heavily notched, demonstrating that the one-dimensional morphology has been substantially destroyed. This pronounced fragmentation greatly increases the grain-boundary density and the degree of structural distortion, which not only enhances phonon scattering and is expected to suppress the lattice thermal conductivity, but also correlates well with the observed bandgap narrowing from 1.27 eV (BiSeI) to 0.98 eV ($BiSe_{0.7}Te_{0.3}I$. The increased structural disorder and more substantial overlap between Bi-p and (Se/Te)-p orbitals at this composition are consistent with a smaller bandgap and improved thermoelectric performance. When the Te content reaches x = 0.5, the $BiSe_{0.5}Te_{0.5}I$ powder is mainly composed of highly fragmented irregular particles (Figure S3e,f); The banded morphology almost completely disappears and is replaced by granular masses. At this point, the structure becomes more uniform, and the number of grain boundaries decreases, leading to weakened interfacial scattering that is not conducive to reducing thermal conductivity or optimizing carrier transport. At the same time, the partial recovery of structural uniformity and the mitigation of excessive local distortion are in line with the slight bandgap widening to 0.99 eV in $BiSe_{0.5}Te_{0.5}I$. Thus, the nonmonotonic evolution of the bandgap (narrowing at x = 0.3 and reopening at x = 0.5) is entirely consistent with the morphology-driven changes in grain-boundary density and structural disorder induced by Te substitution. The corresponding EDS spectrum and elemental mappings for $BiSe_{0.7}Te_{0.3}I$ (Figure 3c–g) show only signals for Bi, Se, Te, and I. A homogeneous distribution of all elements, while Table S1 confirms that the Te content systematically increases at the expense of Se with nearly constant Bi and I content, verifying that Te successfully substitutes for Se on the chalcogen site without forming obvious secondary phases.
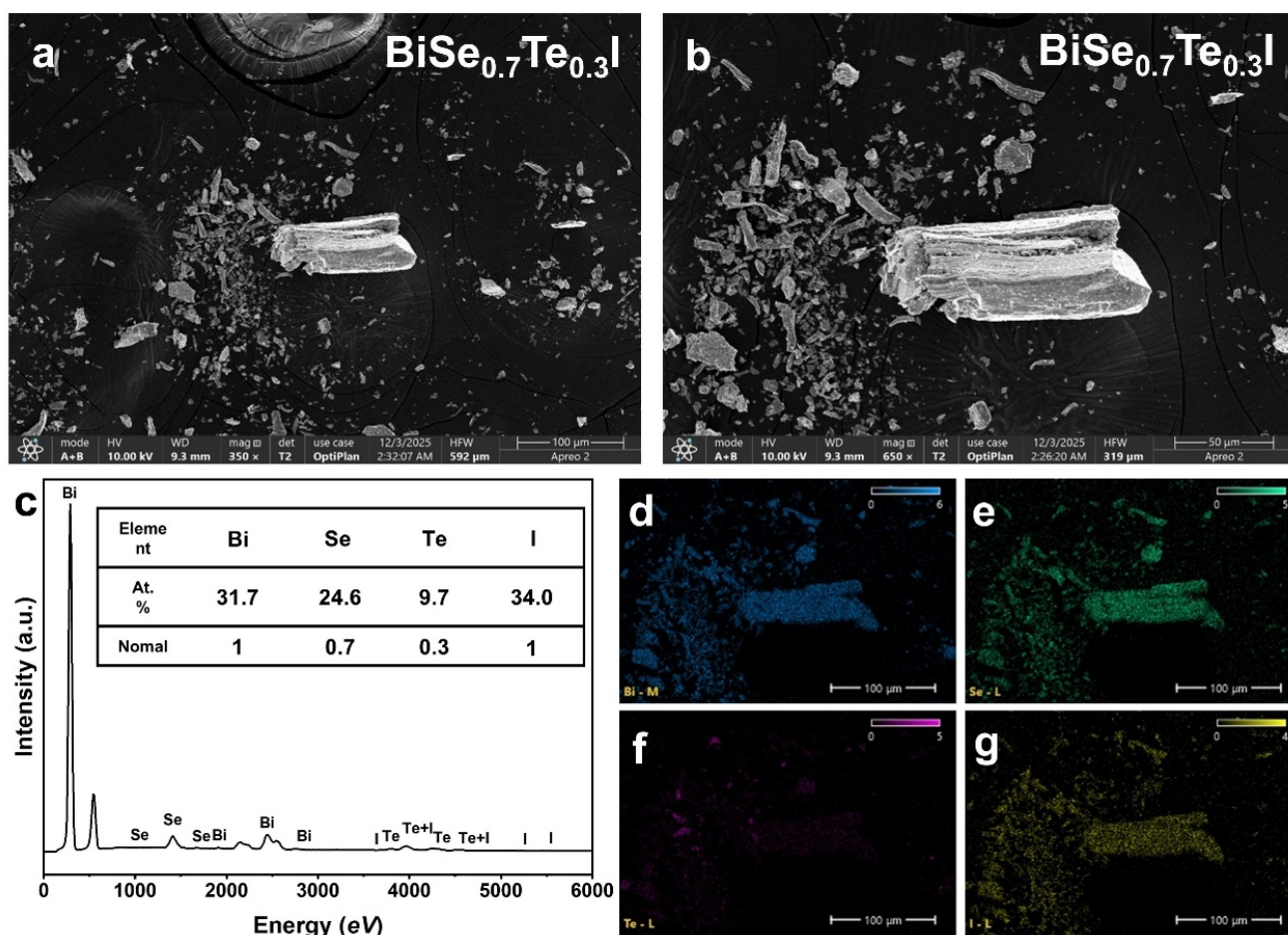
**Figure 3.** SEM and EDS analyses of $BiSe_{0.7}Te_{0.3}I$ powders. (**a,b**) SEM images at different magnifications, showing that partial substitution of Se by Te leads to a two-dimensional plate-like morphology. (**c**) EDS spectrum and corresponding atomic ratios, confirming a composition close to $BiSe_{0.7}Te_{0.3}I$. (**d–g**) Elemental mapping of Bi, Se, Te, and I, respectively, indicates the homogeneous distribution of all constituent elements in the crystal.

## 3.4. Microstructural Evolution and Atomic-Scale Distortion Induced by Te Substitution

To further substantiate the morphology evolution, TEM analyses were conducted on BiSeI and Te-substituted $BiSe_{1-x}Te_xI$ powders (Figures 4 and S4). Pristine BiSeI shows large plate-like particles consistent with the ribbon-like morphology observed in SEM. With light Te substitution ($BiSe_{0.9}Te_{0.1}I$), the particles already exhibit flake-like features, indicating the early onset of ribbon fragmentation. At moderate substitution ($BiSe_{0.7}Te_{0.3}I$), the particles become more severely fractured and irregular, consistent with the pronounced structural disruption seen in SEM. At higher Te content ($BiSe_{0.5}Te_{0.5}I$), the powders evolve into more compact, aggregated flake-like particles, confirming a progressive transition from extended ribbons to fragmented sheets and, ultimately, more consolidated aggregates. High-resolution TEM (HRTEM) images demonstrate that all samples remain highly crystalline, but their interplanar spacings expand systematically with Te doping. Pristine BiSeI exhibits clear lattice fringes with a spacing of ~0.321 nm (Figure 4b), whereas $BiSe_{0.7}Te_{0.3}I$ shows an enlarged spacing of ~0.350 nm (Figure 4e), reflecting lattice expansion due to Te substitution and enhanced structural distortion. Similarly, $BiSe_{0.9}Te_{0.1}I$ and $BiSe_{0.5}Te_{0.5}I$ exhibit spacings of ~0.337 nm and ~0.343 nm, respectively (Figure S4b,e), confirming that Te incorporation introduces local strain while maintaining crystallinity. These nanoscale distortions match the SEM observation that the most severe fragmentation and highest grain-boundary density occur at x = 0.3, which is also the composition exhibiting the smallest bandgap (0.98 eV). The increased lattice disorder and stronger Bi-(Se/Te) p-orbital interactions at this doping level naturally correlate with bandgap

narrowing. Despite the notable morphology evolution and lattice distortion, FFT-processed SAED patterns of all samples (Figures 4c,f and S4c,f) reveal well-defined diffraction spots that can be indexed to the (220), (130), and (210) planes of the BiSeI-type crystal structure. This confirms that Te substitution does not induce a phase transition, but instead produces a solid solution in which the fundamental lattice symmetry is preserved. This structural robustness underscores the preserved crystallographic stability across all Te substitution levels.
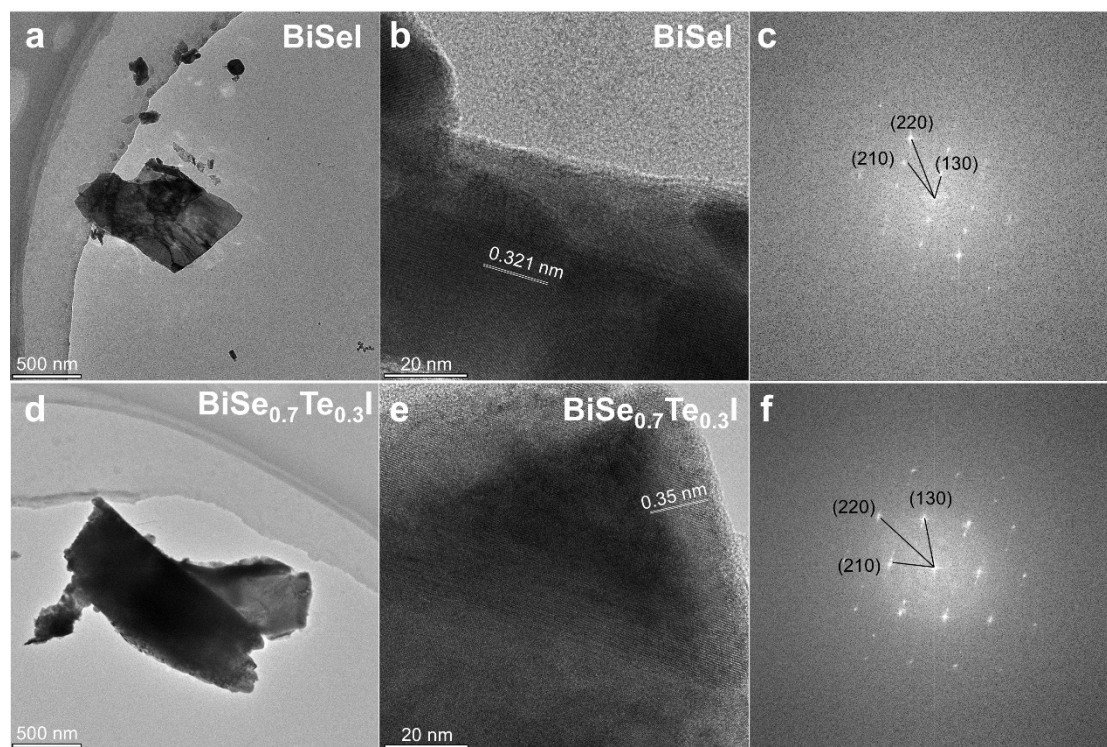


**Figure 4.** TEM characterization of pristine BiSeI and Te-doped $BiSe_{0.7}Te_{0.3}I$ powders. (**a,d**) Low-magnification TEM images showing the plate-like morphology of BiSeI and $BiSe_{0.7}Te_{0.3}I$, respectively. (**b,e**) High-resolution TEM (HRTEM) images displaying clear lattice fringes with interplanar spacings of ~0.321 and ~0.35 nm, evidencing the high crystallinity of both samples. (**c,f**) Fast-Fourier-transform (FFT)-processed selected-area electron diffraction (SAED) patterns obtained from the HRTEM images, where the diffraction spots can be indexed to the (220), (130), and (210) planes of the BiSeI-type structure, confirming that Te substitution preserves the overall crystal structure.

Overall, the TEM analyses corroborate and extend the SEM-EDS findings by showing that moderate Te substitution (x = 0.3) induces the most pronounced structural fragmentation and grain-boundary proliferation, thereby strengthening phonon scattering and corresponding to the minimum bandgap observed in the optical measurements. When the Te content is further increased to x = 0.5, the microstructure becomes partially more uniform, leading to a reduction in grain-boundary density and interfacial scattering, consistent with the slight reopening of the bandgap. Meanwhile, the progressively enlarged lattice spacings detected across the $BiSe_{1-x}Te_xI$ series confirm the presence of Te-induced lattice expansion and disorder, supporting the electronic-structure modulation inferred from the optical absorption spectra. Despite these morphologies and lattice distortions, the SAED patterns reveal that the BiSeI crystal framework remains intact across all compositions, indicating that Te substitution modifies disorder and orbital hybridization without disrupting the material's fundamental phase stability. These TEM results provide atomic-scale evidence for the nonmonotonic interplay among morphology, structural disorder, and bandgap evolution in $BiSe_{1-x}Te_xI$, further clarifying the structure-property relationships governing its thermoelectric behavior.

### 3.5. Enhanced Thermoelectric Transport Properties and Structure-Property Correlation

Building on the above structural, optical, and microstructural characterizations, the thermoelectric transport properties of $BiSe_{1-x}Te_xI$ (x = 0, 0.1, 0.3, 0.5) in the temperature range of 300–400 K were further analyzed. In all cases, the overall performance can be quantified by the dimensionless figure of merit $ZT = S^2\sigma T/\kappa$, where $S$ denotes the Seebeck coefficient, $\sigma$ represents the electrical conductivity, $\kappa$ refers to the total thermal conductivity, and $T$ is the absolute temperature. Of particular relevance is the power factor (*PF*), defined as $PF = S^2\sigma$, while the thermal conductivity ($\kappa$) is closely correlated with the carrier concentration ($n$) and mobility ($\mu$), with $\sigma = ne\mu$, where $e$ is the elementary charge [12], temperature-dependent Hall measurements were further used to quantitatively clarify the origin of the electrical-transport evolution with Te substitution.

As shown in Figures 5a and S7, Te substitution leads to a pronounced enhancement of $\sigma$, and $BiSe_{0.7}Te_{0.3}I$ maintains the highest $\sigma$ throughout 300–400 K. Hall results reveal that this conductivity enhancement is primarily driven by a substantial increase in carrier concentration $n_H$, which rises by nearly two orders of magnitude from ~$10^{17}$ cm$^{-3}$ (BiSeI) to $10^{18}$ cm$^{-3}$ for Te-substituted samples, reaching the $10^{18}$–$10^{19}$ cm$^{-3}$ range for x = 0.3 and 0.5. In contrast, the carrier mobility $\mu_H$ decreases monotonically with increasing Te content, consistent with strengthened alloy/disorder scattering introduced by Te-for-Se substitution. Meanwhile, $\mu_H$ also decreases with temperature for all compositions, indicating that phonon scattering dominates the temperature-dependent transport in this window. Therefore, the composition dependence of $\sigma$ mainly reflects the competition between the strong $n_H$ increase (beneficial) and the mobility degradation (detrimental), yielding an optimal electrical transport at moderate substitution (x = 0.3) where $n_H$ is substantially enhanced while $\mu_H$ remains relatively preserved.
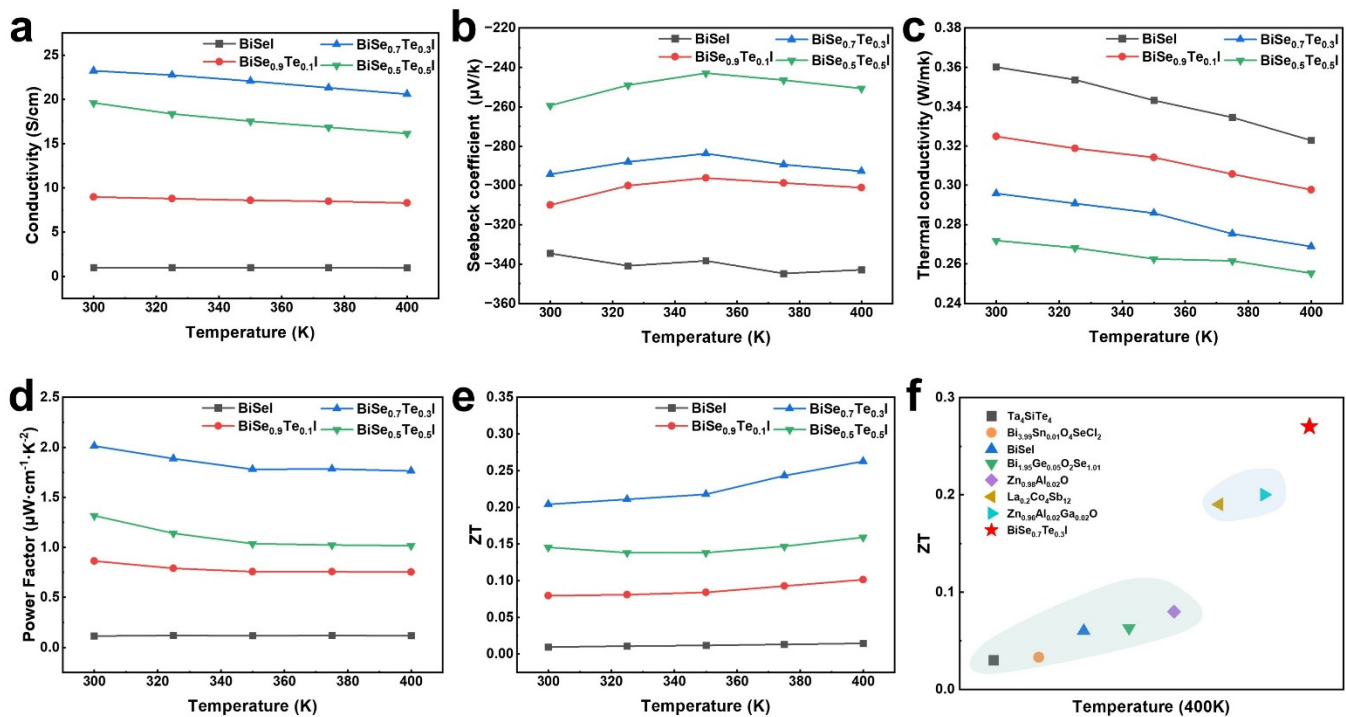


**Figure 5.** Thermoelectric transport properties of $BiSe_{1-x}Te_xI$ (x = 0, 0.1, 0.3, 0.5). (**a**) Electrical conductivity ($\sigma$) of $BiSe_{1-x}Te_xI$ (x = 0, 0.1, 0.3, 0.5) as a function of temperature. The substitution effectively enhances carrier transport, and the $\sigma$ of $BiSe_{0.7}Te_{0.3}I$ remains the highest across the entire temperature range, indicating improved carrier mobility and optimized carrier concentration. (**b**) Seebeck coefficient (*S*) as a function of temperature. All samples exhibit negative *S* values, confirming *n*-type conduction. The |*S*| values first increase and then slightly decrease with temperature, and the $BiSe_{0.7}Te_{0.3}I$ sample reaches the largest |*S*| of approximately 200 $\mu V \cdot K^{-1}$ near 350 K. (**c**) Thermal conductivity ($\kappa$) as a function of temperature. $\kappa$ decreases monotonically with increasing temperature for all compositions. The incorporation of Te significantly suppresses $\kappa$ owing to enhanced phonon

scattering arising from mass fluctuation and lattice distortion between Te and Se atoms. (**d**) Power factor ($PF = S^2\sigma$) versus temperature. The *PF* increases steadily with temperature, and $BiSe_{0.7}Te_{0.3}I$ exhibits the highest *PF* among all samples, demonstrating a favorable balance between electrical conductivity and Seebeck coefficient. (**e**) Temperature dependence of the thermoelectric figure of merit ($ZT = S^2\sigma T/\kappa$). The *ZT* values increase with temperature, with $BiSe_{0.7}Te_{0.3}I$ achieving the maximum value of ~0.27 at 400 K, which is significantly higher than that of pristine BiSeI. (**f**) Comparison of the thermoelectric figure of merit (*ZT*) for representative inorganic thermoelectric materials in the temperature range of 400 K. The $BiSe_{0.7}Te_{0.3}I$ sample demonstrates a competitive *ZT* level in the low-to-medium temperature range compared with reported materials.

The temperature-dependent Seebeck coefficients *S* are negative for all compositions, confirming that electrons serve as the dominant charge carriers. The magnitude |*S*| increases with temperature, reaching a maximum near 350 K before slightly decreasing at higher temperatures. Within the single parabolic band approximation, |*S*| is inversely proportional to the carrier concentration according to the Pisarenko relation: $|S| \propto m^* T/n^{2/3}$, where $m^*$ denotes the density-of-states effective mass [34]. The combination of high $\sigma$ and relatively large |*S*| observed in $BiSe_{0.7}Te_{0.3}I$ suggests that Te substitution not only enhances *n* but may also increase $m^*$ through band-edge reconstruction, such as enhanced band degeneracy [18] or stronger p-orbital overlap, thereby mitigating the suppression of |*S*|. In contrast, at x = 0.5, further increases in *n*, coupled with increased structural disorder, lead to a decline in |*S*|, indicating a deviation from the optimal carrier-concentration regime for maximizing the power factor. Consequently, the peak |*S*| of approximately 200 $\mu V\cdot K^{-1}$ around 350 K in $BiSe_{0.7}Te_{0.3}I$ reflects a composition-dependent optimization among carrier concentration (*n*), effective mass ($m^*$), and mobility ($\mu$).

The evolution of thermal conductivity $\kappa$ with Te content can be elucidated by decomposing $\kappa$ into electronic and lattice contributions, expressed as $\kappa = \kappa_e + \kappa_l$. The electronic component $\kappa_e$ is related to the electrical conductivity $\sigma$ via the Wiedemann-Franz law, $\kappa_e = L\sigma T$, where the Lorenz number *L* is evaluated from the measured Seebeck coefficient, and the lattice term is obtained by $\kappa_l = \kappa - \kappa_e$. where the Lorenz number *L* is evaluated from the measured Seebeck coefficient, and the lattice term is obtained by $\kappa_l = \kappa - \kappa_e$. As shown in Figure S8, Te substitution leads to only a modest increase of $\kappa_e$ (consistent with the enhanced $\sigma$), whereas $\kappa_l$ is markedly suppressed and thus governs the overall decrease of $\kappa$ across 300–400 K. This conclusion is quantitatively supported by Table S2, where the $\kappa_e/\kappa$ ratios remain very small for all compositions: pristine BiSeI shows an almost negligible electronic fraction of only 0.13–0.19%, while Te-doped samples increase to 1.30–1.76% (x = 0.1), 4.05–5.10% (x = 0.3), and 3.19–3.88% (x = 0.5) from 300 to 400 K. These values demonstrate that even in the most conductive sample (x = 0.3), heat transport is still overwhelmingly dominated by the lattice term, and the experimentally observed reduction in total $\kappa$ upon Te incorporation primarily originates from the strong suppression of $\kappa_l$, rather than changes in $\kappa_e$. Such suppression arises from multiple structural effects: (i) Te exhibits a larger atomic mass and radius compared to Se, introducing significant mass fluctuations and local strain fields within the chalcogen sublattice, which effectively scatter mid- and high-frequency phonons [15]; (ii) SEM and TEM analyses reveal a distinct morphological transformation from elongated, one-dimensional ribbon-like grains in BiSeI to shorter, thicker plate-like structures and highly fragmented particles in $BiSe_{0.5}Te_{0.5}I$, accompanied by maximized grain-boundary density and pronounced structural distortion at x = 0.5. These microstructural features introduce additional interfaces that strongly scatter long-wavelength phonons [14]; (iii) HRTEM observations confirm progressive lattice expansion and enhanced structural distortion upon Te incorporation, consistent with softened phonon modes evidenced by red-shifted Raman peaks. Collectively, these mechanisms substantially suppress $\kappa_l$ in Te-doped samples, and compared with conventional $Bi_2Se_3/Bi_2Te_3$-based (Bi–Se–Te) thermoelectrics [35,36], the mixed-anion $BiSe_{1-x}Te_xI$ framework offers a much lower, lattice-dominated thermal conductivity (with $\kappa_e/\kappa$ only ~0.13–5.10% at 300–400 K) together with ~1 eV-class bandgap tunability, enabling a clear $\sigma$–$\kappa_l$ decoupling and effective low-to-mid temperature optimization.

The combined impact of optimized electrical transport and suppressed $\kappa_l$ is reflected in the temperature-dependent behavior of the power factor and the thermoelectric figure of merit *ZT*. The power factor, defined

as $PF = S^2\sigma$, increases monotonically with temperature for all samples due to improved carrier activation, with $BiSe_{0.7}Te_{0.3}I$ exhibiting the highest $PF$ throughout the measured range. This superior performance stems from an optimal combination of carrier concentration and band structure at x = 0.3, where $\sigma$ is significantly enhanced while the absolute Seebeck coefficient $|S|$ remains relatively high—attributable to bandgap narrowing and an increased density-of-states effective mass. When the pronounced reduction in $\kappa_l$ is also considered, the resulting $ZT = S^2\sigma T/\kappa$ rises with temperature and reaches a peak value of approximately 0.27 at 400 K for $BiSe_{0.7}Te_{0.3}I$, which is markedly higher than that of pristine BiSeI. The compositional dependence of $ZT$ thus reflects a nonmonotonic interplay among bandgap narrowing, carrier concentration, and microstructural disorder: moderate Te substitution (x = 0.3) achieves the strongest phonon scattering and most favorable electronic configuration, whereas excessive Te doping (x = 0.5) leads to carrier over-doping and partial re-aggregation of the microstructure, disrupting the delicate balance between $\sigma$, $S$, and $\kappa_l$. Finally, compared with representative inorganic thermoelectric materials operating in the low-to-mid temperature range, the $ZT$ value of $BiSe_{0.7}Te_{0.3}I$ at ~400 K is competitive with that of other $n$-type systems [37–41], highlighting the efficacy of heavy-element Te doping in chalcohalide-halide architectures. The established structure-property relationship, which links lattice expansion, vibrational softening, morphological fragmentation, bandgap engineering, and carrier transport, demonstrates that controlled Te substitution enables concurrent optimization of electronic and thermal transport properties. This offers a clear design strategy for further enhancing thermoelectric performance in BiSeI-based and related mixed-anion layered materials through synergistic band and phonon engineering.

## 4. Conclusions

In this work, we systematically investigated the structural, optical, and thermoelectric properties of $BiSe_{1-x}Te_xI$ (x = 0, 0.1, 0.3, 0.5). Structural analysis via X-ray diffraction and Raman spectroscopy confirms successful Te incorporation and reveals doping-induced lattice distortion. Optical absorption measurements show that Te substitution effectively tunes the bandgap of $BiSe_{1-x}Te_xI$, consistent with band-structure modulation. Morphological observations from SEM and TEM reveal a clear evolution from large one-dimensional ribbon-like grains in BiSeI to shorter, thicker plate-like and highly fragmented particles upon Te substitution, while the underlying BiSeI-type crystal structure is preserved across all compositions. These structural and electronic modifications translate directly into improved thermoelectric performance. Temperature-dependent Hall measurements confirm $n$-type transport and a pronounced increase in carrier concentration with Te substitution, whereas the mobility decreases with temperature, indicating phonon-limited transport. Meanwhile, decomposition of thermal conductivity demonstrates that heat transport is lattice-dominated ($\kappa_e/\kappa \leq 5.10\%$ in 300–400 K) and that Te substitution mainly suppresses $\kappa_l$ via enhanced phonon scattering. As a result, $BiSe_{0.7}Te_{0.3}I$ achieved the highest $ZT$ value of ~0.27 at 400 K, representing a fourfold improvement compared to pristine BiSeI. These findings establish anion alloying as an effective strategy for concurrently optimizing carrier transport and suppressing lattice heat conduction in BiSeI-based mixed-anion systems.

## Supplementary Materials

The following supporting information can be found at: https://www.sciepublish.com/article/pii/905, Figure S1: Multi-view comparison of crystal structures in the $BiSe_{1-x}Te_xI$ series; Figure S2: Enlarged powder XRD patterns ($2\theta = 10$–25°) of BiSeI and Te-substituted $BiSe_{1-x}Te_xI$ (x = 0, 0.1, 0.3, 0.5); Figure S3: Band gap variation of $BiSe_{1-x}Te_xI$ (x = 0, 0.1, 0.3, 0.5); Figure S4: SEM images of BiSeI-based powders with different Te contents; Figure S5: TEM characterization of Te-doped BiSeI powders; Figure S6: Temperature-dependent thermal conductivity of $BiSe_{0.7}Te_{0.3}I$; Figure S7: Temperature-dependent Hall transport parameters of $BiSe_{1-x}Te_xI$ (x = 0, 0.1, 0.3, 0.5) measured in the 300–400 K range; Figure S8:

Temperature dependence of the separated thermal conductivity components for $BiSe_{1-x}Te_xI$ (x = 0, 0.1, 0.3, 0.5) in the range of 300–400 K; Table S1: Elemental compositions of $BiSe_{1-x}Te_xI$ powders determined by SEM–EDS; Table S2: Ratio of electronic thermal conductivity to total thermal conductivity ($\kappa_e/\kappa$, %) for $BiSe_{1-x}Te_xI$ (x = 0, 0.1, 0.3, 0.5) in the temperature range of 300–400 K.

## Statement of the Use of Generative AI and AI-Assisted Technologies in the Writing Process

During the preparation of this manuscript, the author(s) used ChatGPT to improve the language and readability of the text. All content was carefully reviewed and revised by the authors, who take full responsibility for the final content of the manuscript.

## Author Contributions

Z.Z., Z.F. and J.Z. contributed to the study conception and design. Material preparation, data collection and analysis were performed by Z.Z. The first draft of the manuscript was written by Z.Z. Z.Z., Z.F. and J.Z. commented on previous versions of the manuscript. All authors read and approved the final manuscript.

## Ethics Statement

Not applicable.

## Informed Consent Statement

Not applicable.

## Data Availability Statement

Additional data can be provided upon request.

## Funding

## Declaration of Competing Interest

The authors declare that they have no known competing financial interests or personal relationships that could have appeared to influence the work reported in this paper.

## References

1. Wang J, Yin Y, Che C, Cui M. Research progress of thermoelectric materials—A review. *Energies* **2025**, *18*, 2122. DOI:10.3390/en18082122
2. Tan G, Zhao L-D, Kanatzidis MG. Rationally designing high-performance bulk thermoelectric materials. *Chem. Rev.* **2016**, *116*, 12123–12149. DOI:10.1021/acs.chemrev.6b00255
3. Jiang B, Yu Y, Cui J, Liu X, Xie L, Liao J, et al. High-entropy-stabilized chalcogenides with high thermoelectric performance. *Science* **2021**, *371*, 830–834. DOI:10.1126/science.abe1292
4. He J, Tritt TM. Advances in thermoelectric materials research: Looking back and moving forward. *Science* **2017**, *357*, eaak9997. DOI:10.1126/science.aak9997
5. Zhao LD, Lo SH, Zhang Y, Sun H, Tan G, Uher C, et al. Ultralow thermal conductivity and high thermoelectric figure of merit in SnSe crystals. *Nature* **2014**, *508*, 373–377. DOI:10.1038/nature13184
6. Gibson QD, Zhao T, Daniels LM, Walker HC, Daou R, Hébert S, et al. Low thermal conductivity in a modular inorganic material with bonding anisotropy and mismatch. *Science* **2021**, *373*, 1017–1022. DOI:10.1126/science.abh1619

7. Gibson QD, Manning TD, Zanella M, Zhao T, Murgatroyd PAE, Robertson CM, et al. Modular design via multiple anion chemistry of the high mobility van der waals semiconductor Bi$_4$O$_4$SeCl$_2$. *J. Am. Chem. Soc.* **2020**, *142*, 847–856. DOI:10.1021/jacs.9b09411

8. Xu Y, Wang J, Su B, Deng J, Peng C, Wu C, et al. Tightly bound and room-temperature-stable excitons in van der waals degenerate-semiconductor Bi$_4$O$_4$SeCl$_2$ with high charge-carrier density. *Commun. Mater.* **2023**, *4*, 69. DOI:10.1038/s43246-023-00392-1

9. Gibson QD, Newnham JA, Dyer MS, Robertson CM, Zanella M, Surta TW, et al. Expanding multiple anion superlattice chemistry: Synthesis, structure and properties of Bi$_4$O$_4$SeBr$_2$ and Bi$_6$O$_6$Se$_2$Cl$_2$. *J. Solid State Chem.* **2022**, *312*, 123246. DOI:10.1016/j.jssc.2022.123246

10. Zhu YK, Sun Y, Dong X, Yin L, Liu M, Guo M, et al. General design of high-performance and textured layered thermoelectric materials via stacking of mechanically exfoliated crystals. *Joule* **2024**, *8*, 2412–2424. DOI:10.1016/j.joule.2024.05.006

11. Pan Y, Li J-F. Thermoelectric performance enhancement in *n*-type Bi$_2$(TeSe)$_3$ alloys owing to nanoscale inhomogeneity combined with a spark plasma-textured microstructure. *NPG Asia Mater.* **2016**, *8*, e275. DOI:10.1038/am.2016.67

12. Kim HS, Liu W, Chen G, Chu CW, Ren Z. Relationship between thermoelectric figure of merit and energy conversion efficiency. *Proc. Natl. Acad. Sci. USA* **2015**, *112*, 8205–8210. DOI:10.1073/pnas.1510231112

13. Ghosh S, Nozariasbmarz A, Lee H, Raman L, Sharma S, Smriti RB, et al. High-entropy-driven half-heusler alloys boost thermoelectric performance. *Joule* **2024**, *8*, 3303–3312. DOI:10.1016/j.joule.2024.08.008

14. Biswas K, He J, Blum ID, Wu CI, Hogan TP, Seidman DN, et al. High-performance bulk thermoelectrics with all-scale hierarchical architectures. *Nature* **2012**, *489*, 414–418. DOI:10.1038/nature11439

15. Klemens PG. The scattering of low-frequency lattice waves by static imperfections. *Proc. Phys. Soc. Sect. A* **1955**, *68*, 1113–1128. DOI:10.1088/0370-1298/68/12/303

16. Klemens PG. Thermal resistance due to point defects at high temperatures. *Phys. Rev.* **1960**, *119*, 507–509. DOI:10.1103/PhysRev.119.507

17. Peng J, Deskins WR, Malakkal L, El-Azab A. Thermal conductivity of α-U with point defects. *J. Appl. Phys.* **2021**, *130*, 185101. DOI:10.1063/5.0064259

18. Fu C, Bai S, Liu Y, Tang Y, Chen L, Zhao X, et al. Realizing high figure of merit in heavy-band *p*-type half-heusler thermoelectric materials. *Nat. Commun.* **2015**, *6*, 8144. DOI:10.1038/ncomms9144

19. Heremans JP, Jovovic V, Toberer ES, Saramat A, Kurosaki K, Charoenphakdee A, et al. Enhancement of thermoelectric efficiency in PbTe by distortion of the electronic density of states. *Science* **2008**, *321*, 554–557. DOI:10.1126/science.1159725

20. Liu Z, Gao W, Oshima H, Nagase K, Lee CH, Mori T. Maximizing the performance of *n*-type Mg$_3$Bi$_2$ based materials for room-temperature power generation and thermoelectric cooling. *Nat. Commun.* **2022**, *13*, 1120. DOI:10.1038/s41467-022-28798-4

21. Pei Y, Shi X, LaLonde A, Wang H, Chen L, Snyder GJ. Convergence of electronic bands for high performance bulk thermoelectrics. *Nature* **2011**, *473*, 66–69. DOI:10.1038/nature09996

22. Zhao T, Duan S, Dou W, Xu T, Wang X, Bai Y, et al. Edge-dominated epitaxy of topological insulator Bi$_2$Se$_3$ with ultrabroadband response. *ACS Nano* **2025**, *19*, 26055–26064. DOI:10.1021/acsnano.5c06699

23. Zhao C, Tan C, Lien DH, Song X, Amani M, Hettick M, et al. Evaporated tellurium thin films for *p*-type field-effect transistors and circuits. *Nat. Nanotechnol.* **2020**, *15*, 53–58. DOI:10.1038/s41565-019-0585-9

24. Wang Z, Tan C, Peng M, Yu Y, Zhong F, Wang P, et al. Giant infrared bulk photovoltaic effect in tellurene for broad-spectrum neuromodulation. *Light Sci. Appl.* **2024**, *13*, 277. DOI:10.1038/s41377-024-01640-w

25. Das A, Debnath K, Maria I, Das S, Dutta P, Swain D, et al. Influence of subvalent twin-rattler for high *n*-type thermoelectric performance in Bi$_{13}$S$_{18}$Br$_2$ chalcohalide. *J. Am. Chem. Soc.* **2024**, *146*, 30518–30528. DOI:10.1021/jacs.4c11738

26. Ghorpade UV, Suryawanshi MP, Green MA, Wu T, Hao X, Ryan KM. Emerging chalcohalide materials for energy applications. *Chem. Rev.* **2023**, *123*, 327–378. DOI:10.1021/acs.chemrev.2c00422

27. Govindaraj P, Venugopal K. Intrinsic ultra-low lattice thermal conductivity in orthorhombic BiSI: An excellent thermoelectric material. *J. Alloys Compd.* **2022**, *929*, 167347. DOI:10.1016/j.jallcom.2022.167347

28. Ganose AM, Butler KT, Walsh A, Scanlon DO. Relativistic electronic structure and band alignment of BiSI and BiSeI: Candidate photovoltaic materials. *J. Mater. Chem. A* **2016**, *4*, 2060–2068. DOI:10.1039/C5TA09612J

29. Shi H, Ming W, Du M-H. Bismuth chalcohalides and oxyhalides as optoelectronic materials. *Phys. Rev. B* **2016**, *93*, 104108. DOI:10.1103/PhysRevB.93.104108

30. He Y, Zhou J. First-principles study on the ultralow lattice thermal conductivity of BiSeI. *Phys. B* **2022**, *646*, 414278. DOI:10.1016/j.physb.2022.414278

31. Xiong G, Liu T, Huang H, Wang J. Thermoelectric properties of janus BiXI (X = S and Se) monolayers: A first-principles study. *J. Appl. Phys.* **2024**, *136*, 185102. DOI:10.1063/5.0221109

32. Kunioku H, Higashi M, Abe R. Low-temperature synthesis of bismuth chalcohalides: Candidate photovoltaic materialswith easily, continuously controllable band gap. *Sci. Rep.* **2016**, *6*, 32664. DOI:10.1038/srep32664

33. Ran Z, Wang X, Li Y, Yang D, Zhao XG, Biswas K, et al. Bismuth and antimony-based oxyhalides and chalcohalides as potential optoelectronic materials. *Npj Comput. Mater.* **2018**, *4*, 14. DOI:10.1038/s41524-018-0071-1

34. Uher C, Yang J, Hu S, Morelli DT, Meisner GP. Transport properties of pure and doped *M* NiSn (*M* = Zr, Hf). *Phys. Rev. B* **1999**, *59*, 8615–8621. DOI:10.1103/PhysRevB.59.8615

35. Dedi, Lee PC, Wei PC, Chen YY. Thermoelectric Characteristics of A Single-Crystalline Topological Insulator $Bi_2Se_3$ Nanowire. *Nanomaterials* **2021**, *11*, 819–830. DOI:10.3390/nano11030819

36. Qiu B, Sun L, Ruan X. Lattice thermal conductivity reduction in $Bi_2Te_3$ quantum wires with smooth and rough surfaces: A molecular dynamics study. *Phys. Rev. B* **2011**, *83*, 35312. DOI:10.1103/PhysRevB.83.035312

37. Ruleova P, Plechacek T, Kasparova J, Vlcek M, Benes L, Lostak P, et al. Enhanced thermoelectric performance of *n*-type $Bi_2O_2Se$ ceramics induced by Ge doping. *J. Electron. Mater.* **2018**, *47*, 1459–1466. DOI:10.1007/s11664-017-5952-4

38. Park KH, Lee S, Seo WS, Baek S, Shin DK, Kim IH. Thermoelectric properties of La-filled $CoSb_3$ skutterudites. *J. Korean Phys. Soc.* **2014**, *64*, 1004–1008. DOI:10.3938/jkps.64.1004

39. Newnham JA, Zhao T, Gibson QD, Manning TD, Zanella M, Mariani E, et al. Band structure engineering of $Bi_4O_4SeCl_2$ for thermoelectric applications. *ACS Org. Inorg. Au* **2022**, *2*, 405–414. DOI:10.1021/acsorginorgau.2c00018

40. Liu Y, Zhi J, Li W, Yang Q, Zhang L, Zhang Y. Oxide materials for thermoelectric conversion. *Molecules* **2023**, *28*, 5894. DOI:10.3390/molecules28155894

41. Inohara T, Okamoto Y, Yamakawa Y, Yamakage A, Takenaka K. Large thermoelectric power factor at low temperatures in one-dimensional telluride $Ta_4SiTe_4$. *Appl. Phys. Lett.* **2017**, *110*, 183901. DOI:10.1063/1.4982623